Physical decoupling of the GOES daytime 3.9 μm channel thermal emission and solar reflection components using total solar eclipse data

S. D. MILLER

Department of Atmospheric Science, Colorado State University, Ft. Collins, Colorado 80523, USA

Abstract. The spectra of solar and terrestrial emissions are considered largely as being decoupled from one another, such that shortwave (reflectance) and longwave (emissive) radiative properties are often discussed as entirely separate regimes. Instruments having detector pass-bands situated in the region of cross-over near the 3.9 μm atmospheric window (where solar and thermal emissions are of comparable magnitude), however, detect both solar reflection and thermal emission simultaneously during daytime operation. This poses a problem to daytime cloud retrievals which seek to exploit the unique optical properties of liquid water at these near-infrared wavelengths but require measurement of either the solar or the thermal component exclusively. Without *a priori* knowledge of these components, empirical relationships or iterative processes must be applied, often without a practical means of quantifying the errors implicit to them. Here, total solar eclipses are proposed as a physical mechanism to decoupling the two radiative components by effectively removing the reflected solar radiation from the 3.9 μm scene during the eclipse. Considerations for this problem are discussed and comparisons to previous approximations presented.

1. Introduction

In the 'Big Picture' of atmospheric science, a unifying goal shared by the many sub-disciplines is to understand how all the components of the climate system, great and small, convolve and converse in complex and non-linear ways to manifest the ensemble system as we know it. The differential heating of our planet's atmosphere and surface by solar (shortwave) energy serves as the primary driving force to this system. Radiative equilibrium is achieved by re-emitting thermal (long-wave) energy to space and transport of heat from regions of surplus to deficit. All circulations cascading down to smaller and smaller scales, characterised by the dynamics of a rotating fluid, the thermodynamics and chemistry associated with this suspension, and the radiative properties (absorption, emission, and reflection) of the atmosphere and underlying surface, engage in an incessant attempt to maximise the entropy of the system (i.e. achieve a state of mechanical, thermal, and chemical equilibrium). In the highly relevant analogy to systems and control theory, we observe the convolution of internal gains and feedbacks of the Earth's *dynamic* transfer function in the form of weather (high frequency) and climate (low frequency) phenomena.

Clouds play an integral role in this system, as their presence (or absence) dictates

the nature of the radiative exchange in terms of how much energy (shortwave and longwave) enters or leaves the system and where the heating/cooling occurs. In the strictest sense, cloud formation by the condensation of water vapour (in response to either the radiative cooling or mechanical lifting of moist air as dictated by the larger-scale circulation) closes its feedback 'circuit' by in turn influencing the thermal/solar energy fluxes and circulations responsible for its coming to being. It is for this reason that we are so interested learning more about the optical properties (those characteristics which determine interactions with radiation) of clouds. In order to understand their role in the greater system, furthermore, these optical properties must be characterised on the global scale. Clearly, the most appropriate means to this end is the space platform. Environmental satellites equipped with multi-spectral radiometers, for example, can measure global cloud emissions and reflections that are related physically to the optical properties sought.

The spectra of solar and terrestrial emissions are considered generally as decoupled from one another, such that shortwave (reflection) and longwave (emission) radiative properties as measured by satellite are often discussed as entirely separate entities. Cursory examination of the Planck emission spectra for blackbodies with temperatures of 5780 K and 253 K (approximate figures for the Sun and the Earth/atmosphere, respectively) reveals the approximation to hold quite well to first order, with only a small region of overlap between the two curves in the region of Ch. 2. For detector channels in spectral bands well outside of this region (e.g. Ch. 1 visible imagery at 0.65 μm or infrared imagery at 10.7 μm), the concerns for potential contamination by either thermal emission or solar reflection are minimal to negligible. However, an instrument with its detector passband situated within this region of cross-over possesses the inherent capability of detecting both solar reflection and thermal emission (i.e. information during both daytime and night-time) simultaneously).

The 3.9 μm channel (Ch. 2) of the Geostationary Observational Environmental Satellites (GOES) and the 3.7 μm channel of the Advanced Very High Resolution Radiometer (AVHRR) are both situated in an atmospheric window. Figure 1 indicates that the reflected downwelling (assuming a range of surface/cloud albedos from 0.0 to 0.5 and a solar zenith angle of 0°, for example) spectral solar flux is roughly the same order of magnitude as typical upwelling emissive fluxes (the 287 K blackbody curve corresponds to a global mean surface temperature, while the 253 K curve corresponds to the global mean radiating temperature of the Earth/atmosphere system in radiative equilibrium). It is for this reason that clouds in Ch. 2 usually appear brighter (warmer) than the underlying surface during the day and darker (cooler) at night (demonstrating properties of both the visible and infrared channels).

Because most retrieval algorithms seek to minimise the number of extraneous variables (e.g. unretrieved quantities which must be specified *a priori* and invariably add additional uncertainty to the results) whenever possible, the use of Ch. 2 during the daytime has largely been avoided by the research community due to the many uncertainties associated with a simultaneous reflecting and emitting scene. There have been a number of previous attempts to decouple the solar and thermal components of the Ch. 2 radiance for the purpose of cloud optical property retrievals. These include empirical relationships (Coakley and Davies 1986), physical relationships (Kaufman and Nakajima 1992, Kidder *et al*. 1998), iterative/correlative approaches (Ou *et al*. 1993, Rao *et al*. 1995), and temporal differencing (Kleepsies 1995). Applications to surface reflectance decoupling are treated by Becker and Li 1990 and Li and Becker 1993 by means of a temperature-independent spectral index.
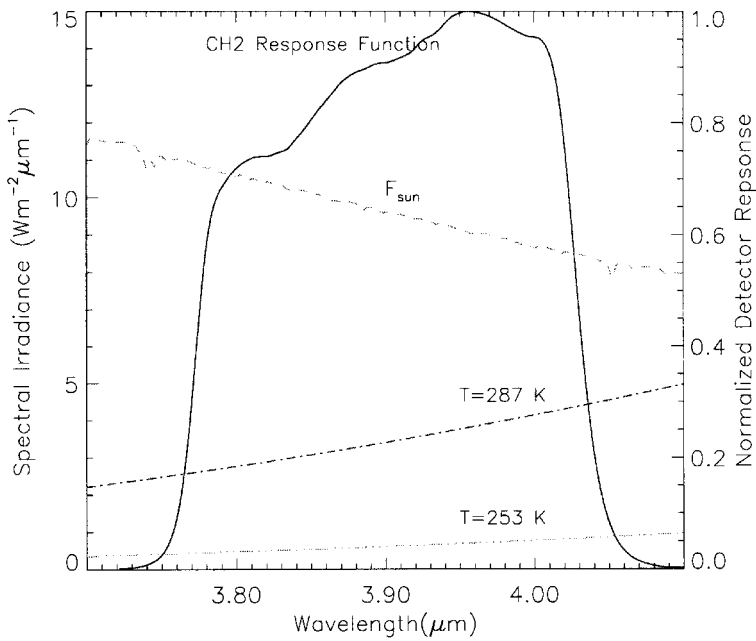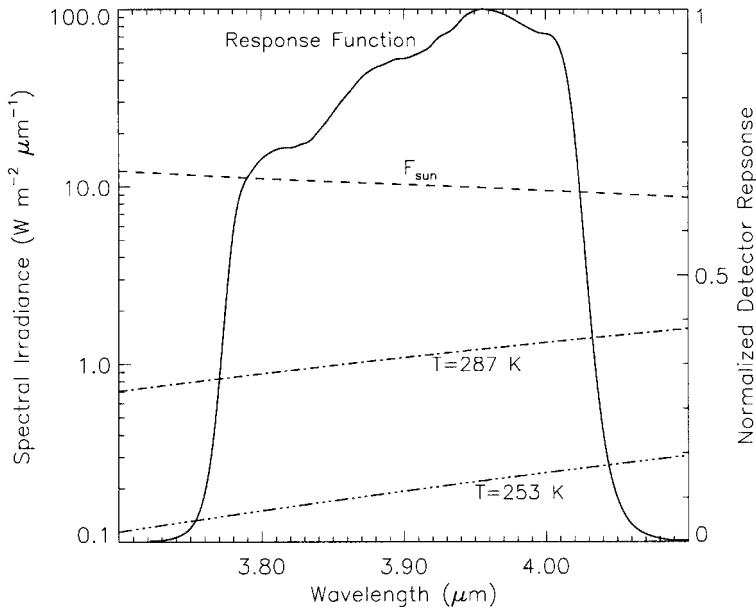
Figure 1.   Solar/thermal contributions to the GOES 3.9 μm channel.

Unfortunately, observational validation data are not available to any of these methods, and hence the errors associated with implicit assumptions that exist in each cannot be quantified readily.

If it were a simple matter of using the observed brightness temperature at an

infrared channel not affected by solar radiation (e.g. 10.7 μm) to compute an equivalent blackbody radiance in Ch. 2, the near-infrared channel problem would have been solved long ago and no doubt we would be much further along in our efforts to develop a global cloud optical property climatology. The reason that the approximation fails is that the surface, atmosphere and clouds themselves are not true blackbody emitters at either wavelength (i.e. the emissivities of the scene components are non-uniform grey-bodies that are seldom equal to unity). For this reason we cannot subtract an inferred 3.9 μm equivalent blackbody radiance based on the 10.7 μm blackbody brightness temperature to remove the thermal component from the former channel, even for the most optically thick of clouds.

This begs the question, 'Does there exist a physical means to decoupling the solar reflection and thermal emission from a given cloudy scene without invoking *any* implicit assumptions about the cloud optical properties?' This would require essentially the ability to 'turn the Sun off' over the area of interest such that the temporal difference between the measurements would isolate unambiguously the solar component. This seemingly impossible experiment can in fact be performed using the geostationary satellite platform and an opportunistic alignment of celestial bodies. To first-order, passage of the moon's umbral shadow (corresponding to the region of complete blockage of the visible solar disc) across the Earth's surface during a total solar eclipse removes the solar reflection component of the field, and often at very low solar zenith angles. Here, we propose to make use of these rare but predictable events to address the solar/thermal decoupling problem.

2. Outline of method

The procedure followed to investigate the 3.9 μm radiative decoupling problem is outlined as follows. First, a collection of solar eclipses over the period where operational geostationary having a 3.9 μm channel was assembled and prioritised according to satellite-coverage and the availability of 3.9 μm data. The exact coordinates and times of these eclipse paths were obtained from a canon of solar eclipse data (Espenak 1998). GOES imagery were then procured from the Cooperative Institute for Research in the Atmosphere (CIRA) satellite archives for the desired spatial and temporal coverage (geostationary platforms are preferred for this application, as they provide before-and-after cloud scenes at a fixed observer geometry). The images, which were available at 30 minute intervals, were sectorised to the large-scale regions of interest, and candidate cases along the eclipse path were identified from the visible imagery. The imagery were then re-sectorised to these local-case regions. Decoupling of the 3.9 μm radiative components was accomplished by temporal differencing of the pixel data about the umbral shadow passage.

Additional experiments to examine the decoupled radiative components of the Ch. 2 imagery were also performed. These included comparisons between true and first-order-estimated (using 10.7 μm brightness temperature and assuming the clouds to behave as blackbody emitters) thermal components, a simple cloud detection algorithm incorporating the method of Rao *et al.* 1995, and an assessment of the performance of previous studies which seek to eliminate either the solar or thermal component from Ch. 2 without *a priori* knowledge of its actual value using various parameterisations/approximations founded on simplified radiative transfer theory and/or empirical relationships. An additional quantity, the 3.9 μm shortwave albedo physical estimate (Kaufman and Nakajima 1992, Kidder *et al.* 1998) is examined, and an example of a physical cloud property retrieval based on these data is

presented. While this analysis encompasses only a small subset of many potential applications, it provides a first-attempt toward addressing by means of solar eclipse data the many lingering questions that exist regarding interpretation cloud reflectance in daytime 3.9 μm satellite imagery.

3. Background

3.1. *Solar eclipses: a brief overview*

Solar eclipses of our era are part of the Saros Series 130 family which began in 1096 and terminates in 2394. After the current series is completed, the entire cycle repeats with identical eclipse groundpaths shifted by roughly 8 hours (or westward one-third of the way around the globe). A total solar eclipse occurs when the moon covers completely the visible solar disc. This region is termed the umbral shadow, with the penumbral shadow encompassing all areas where only partial eclipse occurs. For this reason the total eclipse cannot be regarded as an ideal 'on-off' switch of the Sun, but rather a gradual approach to and from totality through the prenumbral shadow field. The path of totality defines the path of the umbral shadow across the surface of the Earth. Its northern and southern limits define the region of interest to this work. If the Earth–Moon distance is too great, then the umbral shadow will not reach the Earth's surface and an annular eclipse (appearing as a solar disc ring) results. A hybrid eclipse occurs when the umbral shadow does not reach the surface of the Earth on the fringe ends of the path, and an annular→total→annular transition is observed. For this study, only regions within the full umbral shadow of a total eclipse were considered.

The evolution of a total eclipse as observed from a point on the Earth's surface within the path of totality is described often in terms of four so-called 'contact points' between the lunar and solar discs. These are defined from first instance of partial eclipse (1), first instance of total eclipse (2), last instance of total eclipse (3), and last instance of partial eclipse (4). The area between contact points 2 and 3, within the period of totality, is the region of interest for this study. An example of the level to which downwelling solar flux is extinguished within the umbral shadow of a total solar eclipse is illustrated in figure 2. During totality (i.e. between the second and third contact points as indicated in the figure) the downwelling diffuse solar flux has been reduced by nearly four orders of magnitude (from 10 000-lux down to ∼ 3-lux, or roughly 10 times the luminosity of a full moon observed at night). Typical durations of total eclipses are on the order of a few minutes, as the umbral shadow races across the Earth's surface at ground speeds on the order of several kilometres per second. The point of greatest eclipse is defined where the axis of the Moon's shadow passes closest to the centre of the Earth.

3.2. *Applications of the 3.9 μm channel*

Retrieval algorithms that take advantage of the spectrally variant optical behaviour of cloud water and particle size distributions benefit most from imagery that is not contaminated or obscured by additional unretrieved quantities such as the atmospheric gas profile. As the majority of the infrared atmospheric spectrum is devoid of regions where a relatively clear view of the surface and lower-level clouds is available, 'window regions' (spectral bands where absorption and emission by interstitial atmospheric gases is small) are coveted highly by many remote sensing applications. An immediate application of these windows to satellite remote sensing is the ability to retrieve cloud properties including optical depth (characterising
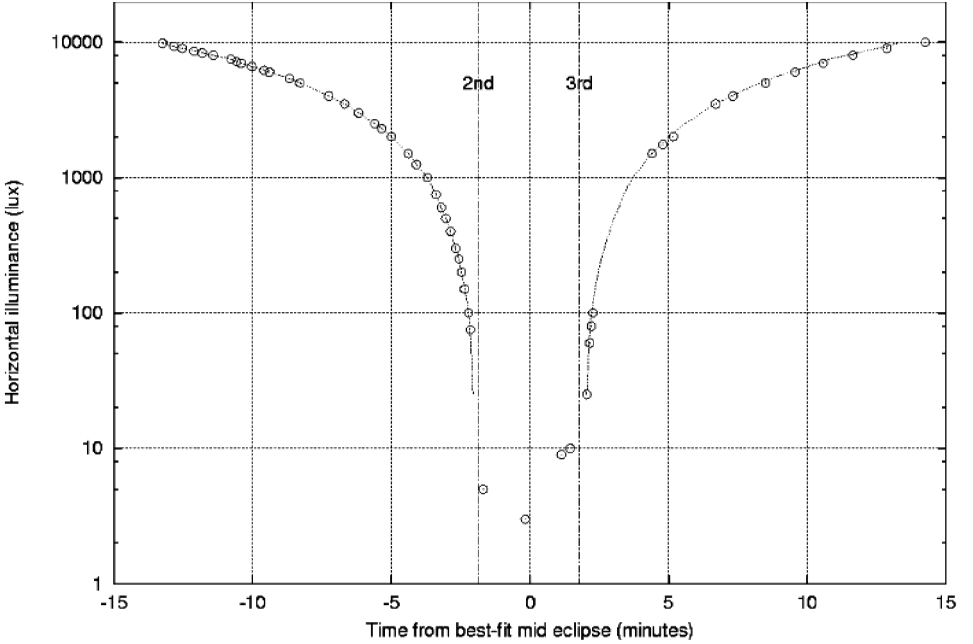
Figure 2. The luminous intensity of downwelling solar radiation at the surface as measured during the passage of the 26 February 1998 total solar eclipse at the Peninsula de Paraguana, Venezuela (12.15 N, 70 W). The times of second (18:09:17) and third contact points (18:12:56) (see text for details) are shown (from Mason and James 1998).

the transmission of light along a path), τ, and effective particle radius (characterising the cloud particle size distribution), r_{eff}. These parameters are defined, respectively, as

$$\tau = \int_{z_1}^{z_2} \sigma_{ext} dz \qquad (1)$$

where σ_{ext} is the volume extinction coefficient of the medium (due to cloud, gas, and aerosol), and

$$r_{eff} = \frac{\int_0^\infty r^3 n(r) dr}{\int_0^\infty r^2 n(r) dr} \qquad (2)$$

where $n(r)$ is the particle size distribution and r is the particle radius (following Hansen and Travis 1974).

To illustrate this concept, radiative transfer theory for liquid water clouds predicts that cloud reflection at visible (non-absorbing by liquid water) wavelengths is largely a function of cloud optical depth, whereas the reflection at a middle-infrared (MIR, defined here as 1.3 to 4.0 μm) wavelength is more dependent on the cloud particle size distribution. This is due to the stronger absorption by liquid water at 3.9 μm (with an imaginary index of refraction $k \sim 10^{-3}$) compared to at 0.65 μm ($k \sim 10^{-9}$). Figure 3 exemplifies this relationship as applied to the simultaneous retrieval of τ and r_{eff} from a pair of simultaneous spectral radiometer observations. Of note is that the orthogonality (and hence, uniqueness) of this relationship fails for optically thinner clouds and at smaller effective radii. Nevertheless, this orthogonality is
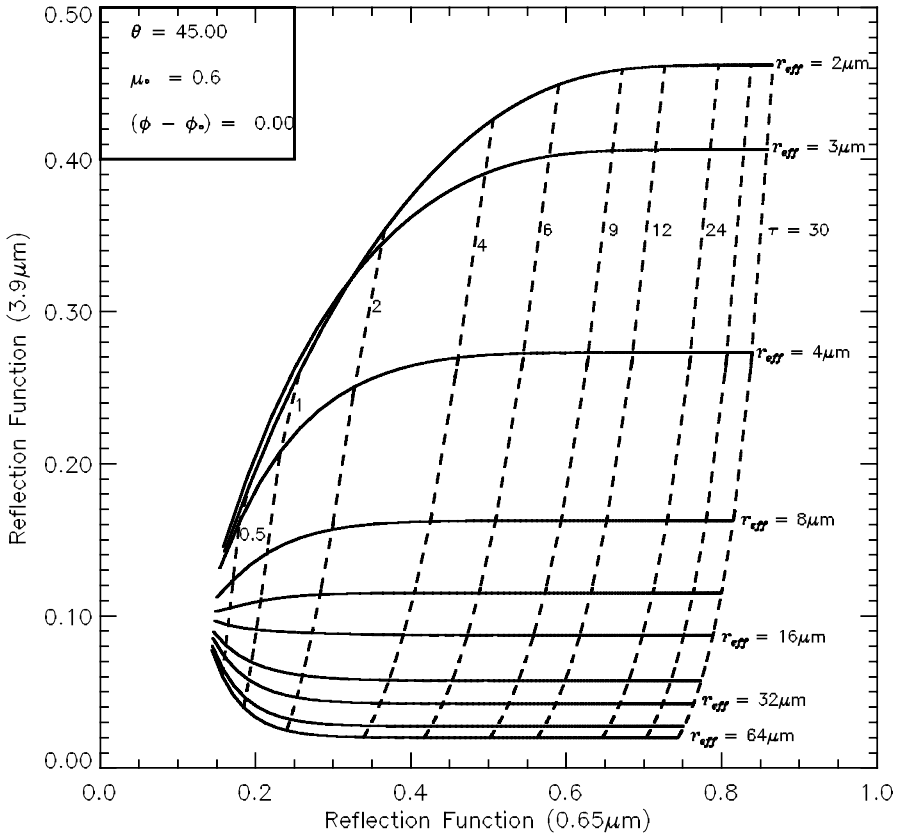
Figure 3. The bi-directional reflection function grid retrieval approach (following Nakajima and King 1990).

superior to that achieved by the shorter-wavelength MIR channels centred about 1.6 and 2.2 μm. For this reason, the 3.9 μm window region (well into the MIR and the last available window channel before water vapour absorption again begins to obscure the atmospheric profile) is used widely in practice.

3.3. *Review of spectral emittance*

Before proceeding to data processing and the discussion of findings, it is important to first refresh ourselves with the relevant radiation principles for clouds in the GOES 3.9 μm and 10.7 μm (channels 2 and 4, respectively) bands of the atmospheric emission spectrum. Long ago, Max Planck discovered that a pure blackbody (having a broadband emissivity of unity) at temperature T and wavelength λ will emit an amount of spectral radiance $B_\lambda(T)$ (W m^{-2} sr^{-1} μm^{-1}) equivalent to

$$B_\lambda(T) = \frac{2hc^2}{\lambda^5(exp(hc/K_b\lambda T) - 1)} \tag{3}$$

where h and K_b are Planck's and Boltzman's constants, respectively. This equation defines the maximum amount of radiation that *any* object with temperature T can emit, and this T is termed the 'equivalent blackbody temperature'. In general, clouds

are considered as non-uniform grey-bodies, such that they emit more like a blackbody at some wavelengths and less-so at others across the spectrum:

$$B_\lambda(T) \rightarrow \varepsilon_\lambda B_\lambda(T), \quad (0.0 \leqslant \varepsilon \leqslant 1.0). \tag{4}$$

where an emittance ε of unity defines the true blackbody radiation.

For the following discussion, we consider for simplicity a night-time cloud scene (with only thermal emissions contributing to the 3.9 μm radiation) as observed by a passive satellite radiometer. For water clouds in the Ch. 2 region, $\varepsilon_\lambda \sim 0.7$, while at Ch. 4, $\varepsilon_\lambda \sim 1.0$. Despite the fact that the cloud does not emit as a pure blackbody in either band, brightness temperatures are often considered as representative of the ambient cloud temperature (even for the most optically thick clouds which block emissions from the warmer underlying surface and atmosphere).

Due to the differences in spectral emittance alone, a cloud with a high absorption optical depth will exhibit a brightness temperature (T) more representative of a blackbody emitter (i.e. a higher spectral radiance) at the ambient temperature of the cloud in Ch. 4 than in Ch. 2. We expect the brightness temperature difference (BTD, Ch. 4–Ch. 2) in this case to be a positive quantity. Conversely, the lower emittance (absorptance) of cloud particles in Ch. 2 translates to a higher cloud transmissivity. For optically thin clouds, a *larger* component of the warmer emissions from the surface and atmosphere below the cloud will reach the satellite in Ch. 2. With the cloud appearing more opaque in Ch. 4 due to its higher emittance, transmission from below is less and the scene will appear cooler than at Ch. 2. As a result, the BTD will be negative for most cirrus clouds (residing in cooler environments and generally having lower optical thickness due to the structure of scattering phase function for ice crystals). This phenomenon of negative BTD cirrus holds for cirrus produced by deep convection through the same principle; the net emission measured by Ch. 2 comes from a lower (warmer) level within the cloud than that of Ch. 4 (i.e. seeing 'deeper' into the convective cloud). Lower-level clouds having ambient temperatures closer to those of the surface, on the other hand, will not display a negative BTD. This discussion is substantiated by Kidder *et al.* 1998, who demonstrate these principles in a 3.9 μm albedo product which, based on these same principles, yields bright (positive values) lower-level clouds and 'black cirrus' (negative values) in night-time GOES imagery. An illustration of this concept is also provided in the results section of this paper.

3.4. *Principles of radiative decoupling*

Neglecting atmospheric emission, the GOES Ch. 2 pre-eclipse (daytime) radiance can be expressed in terms of its reflected and transmitted solar thermal components according to

$$I_{3.9} = t_{3.9}(\text{sun, cld}) t_{3.9}(\text{cld, sat}) \frac{\mu_o F_o}{\pi} \rho_{3.9,\,\text{cld}}$$

$$+ t_{3.9}(\text{sun, sfc}) t_{3.9}^2(\text{cld}) t_{3.9}(\text{sfc, sat}) \frac{\mu_o F_o}{\pi} \rho_{3.9,\,\text{sfc}}$$

$$+ t_{3.9}(\text{cld, sat}) \varepsilon_{3.9,\,\text{cld}} B_{3.9}(T_{\text{cld}})$$

$$+ t_{3.9}(\text{sfc, sat}) t_{3.9}(\text{cld}) \varepsilon_{3.9,\,\text{sfc}} B_{3.9}(T_{\text{sfc}})$$

$$+ \text{H.O.T.} \tag{5}$$

where $t_{3.9}(a, b)$ terms are clearsky transmittances along the path $\overline{ab}$ (with slant-paths considered); F_o and μ_o are the solar spectral flux (top of atmosphere) and cosine of the solar zenith angle, respectively; $B_{3.9}(T)$ is the Planck function describing the spectral emission of a blackbody at temperature T; i.e. $\varepsilon_{3.9}$ is the spectral emissivity; and H.O.T. are higher-order-terms arising from multiple scattering of solar radiation. Contributions by the latter are shown by Tanré 1982 to be minimal at 3.9 μm. The cloud transmittance ($t_{3.9}(\text{cld})$) is a function of optical depth ($\tau_{3.9}$) and zenith angle (μ) given by

$$t_{3.9}(\text{cld}) = e^{-\tau_{3.9}/\mu} \tag{6}$$

During the total eclipse, all terms involving F_o are removed and only the emission terms remain. To good approximation over ocean surfaces $\rho_{3.9,\,\text{sfc}} \to 0.0$, and so this term also departs from equation (5). Assuming also no change in the thermal field between the two times, the difference between the two measurements $I_{3.9}(\text{sol}) = I_{3.9} - I_{3.9,\,\text{eclipse}}$ can be used to solve for the 3.9 μm cloud reflectivity as

$$\rho_{3.9}(\text{cld}) = \frac{I_{3.9}(\text{sol})}{t_{3.9}(\text{sun, cld}) t_{3.9}(\text{cld, sat}) \mu_o F_o / \pi} \tag{7}$$

This defines the bidirectional reflection function, which assumes implicitly the property of isotropic (Lambertian) cloud reflection.

4. Case study

The case that best satisfied all coverage and instrument requirements for this study was the total eclipse of 26 February 1998 (figure 4). The eclipse track began at 1546 Z in the Central Equatorial Pacific (roughly 3000 km south-east of Hawaii), progressed eastward across the Panama/Columbia border (reaching greatest eclipse at 1728 Z off the Pacific coastline of Central America with a 4 minute, 8 second duration of totality at greatest eclipse), and terminated at 1909 Z off the Atlantic coast of Northern Africa. This case featured extensive coverage by GOES satellites (GOES 9 centred at 135 W longitude, GOES-K at 106 W, and GOES-8 at 75 W). The path of totality crossed several areas of tropical convection and cirrus over the equatorial Pacific as well as frontal cloudiness in the mid-Atlantic. The GOES-K satellite (awaiting the failure of GOES-8, but eventually replacing GOES-9 and assuming its current identity of GOES-10) provided the best nadir view of the eclipse path, and was therefore chosen for this study. The fields of view for these satellites are chosen for this study. The fields of view for these satellites are shown in figure 5. Cases for GOES-8 also exist and were analysed, but in the interest of brevity, only the GOES-K results are presented here.

The GOES data were available at 30 minute intervals, with the GOES-K schedule providing imagery upon the hour and half-hour. These data were obtained from CIRA archives. The gradual decrease of solar insolation due to the advancing penumbral shadow necessitated 1 hour time differences to decouple sufficiently the radiative components. While an approximation to the ideal instantaneous 'snap-shot' experiment, it is nonetheless the best afforded by nature. Because of this delay, the main concern for this experiment was the possibility of a changing 3.9 μm thermal field over this time span. These changes are due primarily to the formation, dissipation, and advection of clouds. In cases of marine stratus, this may not be as great of a concern, but in the presence of tropical convection, cirrus, and frontal clouds,
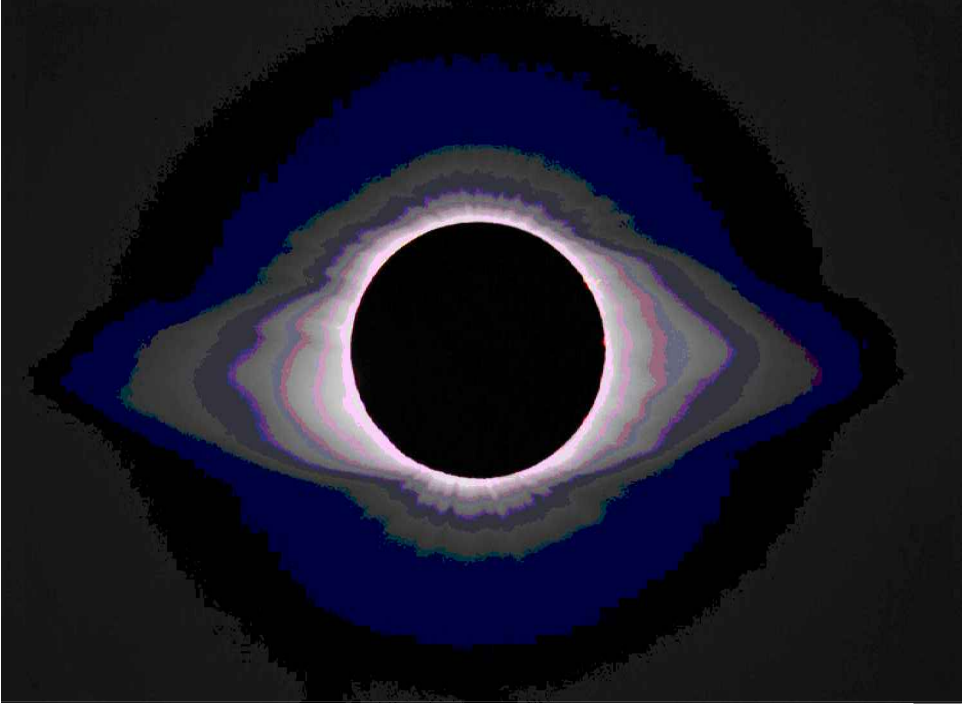
Figure 4.   Photograph during totality of the 26 February 1998 solar eclipse (photograph by
F. Espenak).

extreme caution must be exercised when working with the temporally-differenced
data.

5.   General discussion
5.1.   *Image interpretation*

First, large-scale sectors were extracted from the GOES-K imagery and time
loops constructed to identify local candidate cases. The case points were restricted
to a finite set of positions defined by the satellite image acquisition times (GOES
rapid scan operation-mode was not dedicated to this event). Figure 6 shows the
26 February 1998 eclipse path as observed by the GOES-K visible channel. The
progression of the eclipse is shown at 1 hour resolution (the time interval used to
decouple the Ch. 2 scene). While the available 30 minute resolution compromises
the assumption of a stable thermal field background, the penumbral shadow man-
dated the longer time intervals to obtain a full solar reflection component. Satellite
visible counts fell to values well below instrument calibration within the umbral
shadow itself, with even the brigthest clouds observed to vanish entirely from the
scene along the path of totality.

To illustrate the temporal pixel-differencing approach, GOES visible imagery
were differenced according to

$$I(0.65 \,\mu\mathrm{m}, \mathit{diff}) = I(0.65 \,\mu\mathrm{m}, t_1) - I(0.65 \,\mu\mathrm{m}, t_2) \tag{8}$$

where t_1 is an image prior to eclipse and t_2 is the same registered scene during the
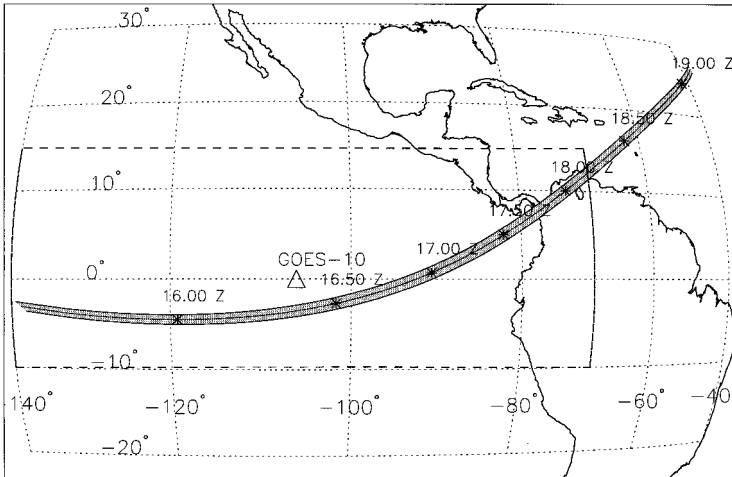umbral shadow passage. An exmaple of this procedure for a subsection of

Figure 5. GOES-K coverage of the 26 February 1998 eclipse. The boxed region designates imagery sectors obtained for all channels, the triangle defines the sub-satellite point, and the curve outlines the eclipse track with selected positions/times labelled.

GOES-K imagery is shown in figure 7. The top two panels display the region observed at half-hour intervals during passage of the umbral shadow, and the lower panel displays the temporal-difference between these two images according to equation (8). Regions to the east, which originally were illuminated at t_1 and darkened with the approaching shadow at t_2, appear bright (positive) in the pixel-differenced image. Conversely, regions to the west/south-west which changed from dark to light as the eclipse advected eastward resulted in a dark (negative) differenced result. The ocean suface, owing to its small visible albedo, does not display the strong radiance differences observed over cloudy areas. Solar/satellite zenith (μ_o) and azimuth angles were computed by spherical geometry using the (latitude,longitude,time,day) information associated with each registered GOES pixel. Spectral solar flux data at 1 nm resolution were convolved with GOES-K Ch. 2 spectral response functions (see figure 1) to obtain the band-integrated solar flux. All Ch. 2 transmission functions were computed from a 16-stream doubling and adding radiative transfer code using a McClatchey tropical profile. The model, described at length in Miller *et al.* 1999, has been equipped to simulate GOES imager channels. Gaseous absorption across the GOES bands was incorporated into the forward model from the correlated-K parameters of Kratz 1995.

5.2. *Umbral advection correction*

An important component to the subsequent analysis of the eclipse data was the accurate identification of the umbral shadow location on the images. Ostensibly, with a reliable data base of eclipse positions/times and the knowledge of the satellite image recording times it would seem a straightforward exercise simply to map out the positions from the data upon the image. An unforeseen problem was encountered, however, as the umbral shadow was observed to be offset eastward to varying magnitude (less-so near the point of greatest eclipse and more-so near the tangent points of the umbral shadow with the surface) from its predicted positions in all the visible imagery. It was soon realised that this was due not to errors in the predicted
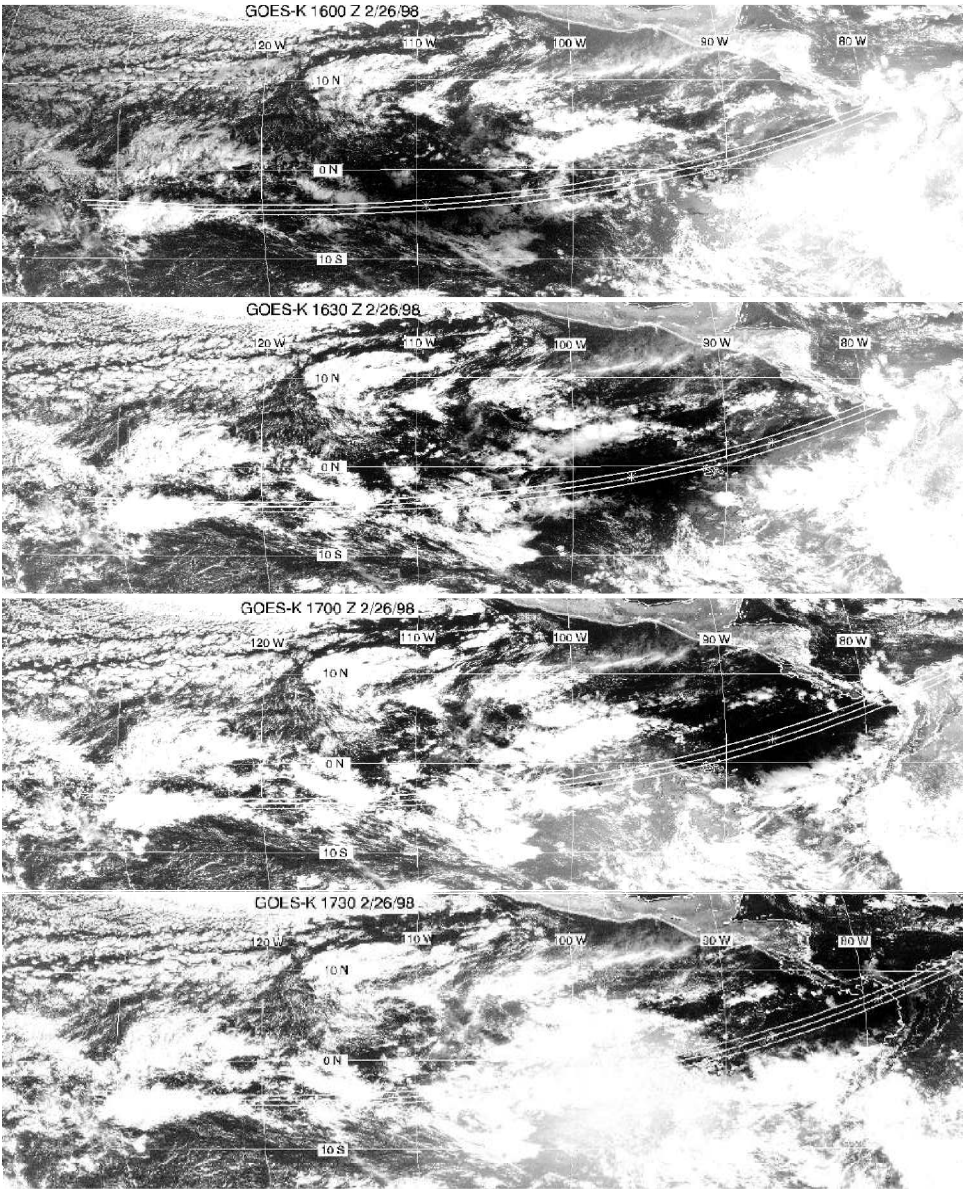
Figure 6.   26 February 1998 eclipse progression as seen from GOES-K.

eclipse position data, but rather to the mechanical scanning operation of the GOES instrument itself when considering the ground speed and acceleration properties of the umbral shadow.

   The GOES imager creates an image by performing successive east–west oriented line scans of a scene (with thousands of picture elements along each line), such that by the time the last line of the scene is scanned in a full-disc image several minutes have elapsed since the start of the scan. While the nominal time of the image is stamped as the time of the *first* scan line, the scans performed close to the equator (near eclipse track) are on the order of 10 minutes offset. While this is not a major
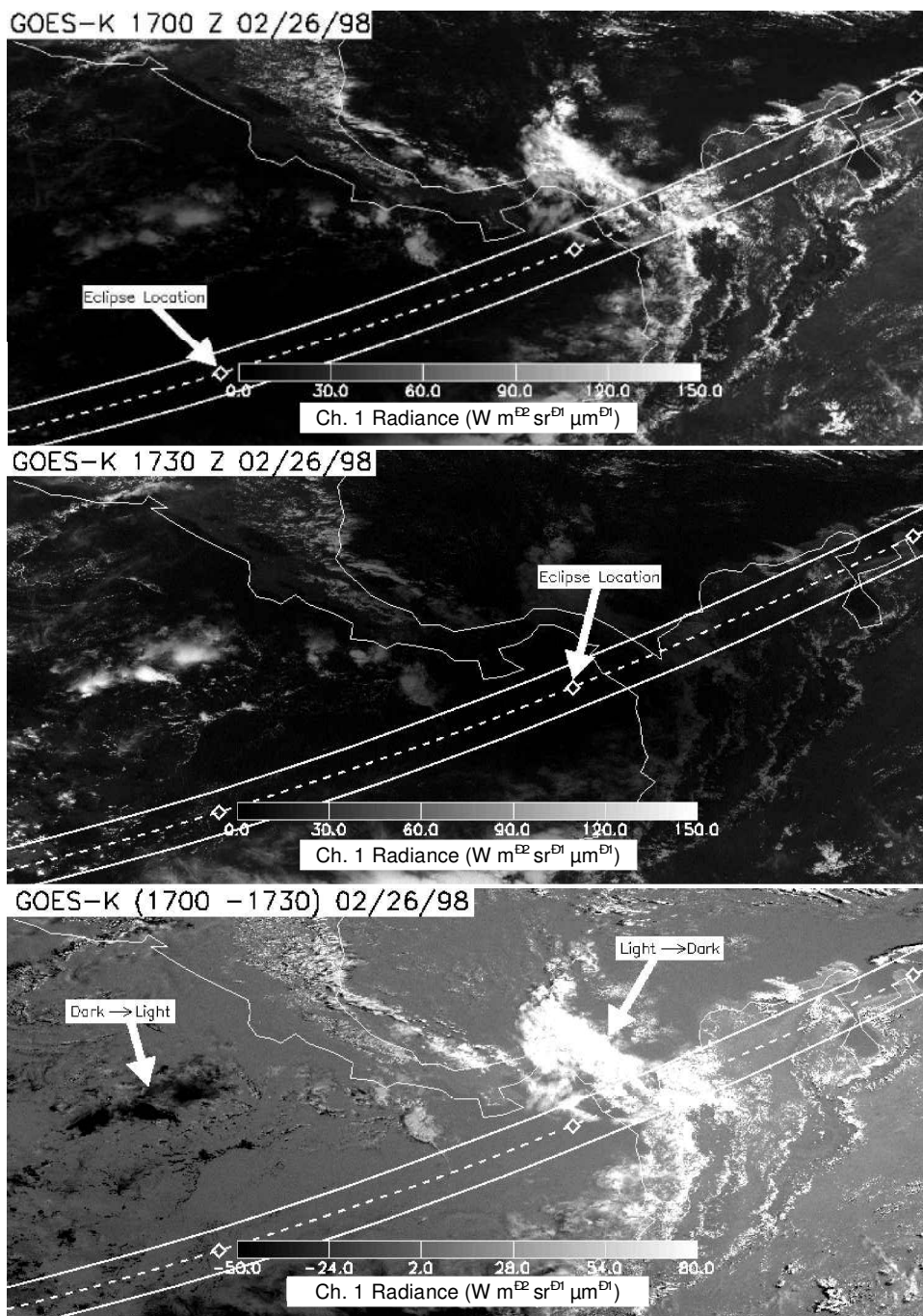
Figure 7. Temporal channel differencing example (GOES-K VIS).

consideration for most atmospheric motions (on the order of tens-of-metres per second) of interest, it presents a serious problem for tracking the umbral shadow. With a ground speed varying from $0.5\,\mathrm{km\,s}^{-1}$ at greatest eclipse upwards to

$4.0 \, \mathrm{km \, s^{-1}}$ near the tangential points, the observed shadow position may be offset by several hundred kilometres from the position suggested by the nominal image scan time. The result is an apparent phase-lead in the imagery which compromises the very important need to define precisely the true location of the umbral shadow.

To reconcile this error, an 'umbral advection correction' was performed by minimising a cost function given by:

$$\sigma^2 = (t_{scn} - t_{ecl})^2 + (\phi_{scn} - \phi_{ecl})^2 \tag{9}$$

where $(t_{scn}, t_{ecl}, \phi_{scn}, \phi_{ecl})$ are the times and longitudes of the instrument scans and the eclipse position database, respectively. Because the eclipse tracks from west to east, a unique (time, longitude) pair exists for each point. Where σ is minimised defines the appropriate eclipse position to apply the image. Figure 8 illustrates the correction as applied to a GOES-8 Ch. 1 image. It is clear that the umbral shadow has moved far from its original position when the scan began. The correction is much larger at the beginning and ending of the eclipse path because the umbral shadow ground speed is much larger in these regions. The correction appears to define accurately the true position of the umbral shadow in the GOES imagery. In this fashion, the corrected central positions for the umbral shadow in the imagery were calculated for all channels and times.

6. Results

The ensemble imagery were searched for incidences where clouds existed near the umbrally-corrected positions. A localised GOES-K region satisfying this criterion is shown in figure 9. The region also happened to be very close to the point of greatest eclipse. Over the period between 1630 Z and 1730 Z, the total eclipse approached an extensive cloud field from the south-west. Loops of the imagery revealed the cloud field to be quasi-stationary over the entire duration of the eclipse passage. Because its brightness temperatures were not much cooler than those of the underlying ocean surface even in regions of highest visible reflectivity (optically thick
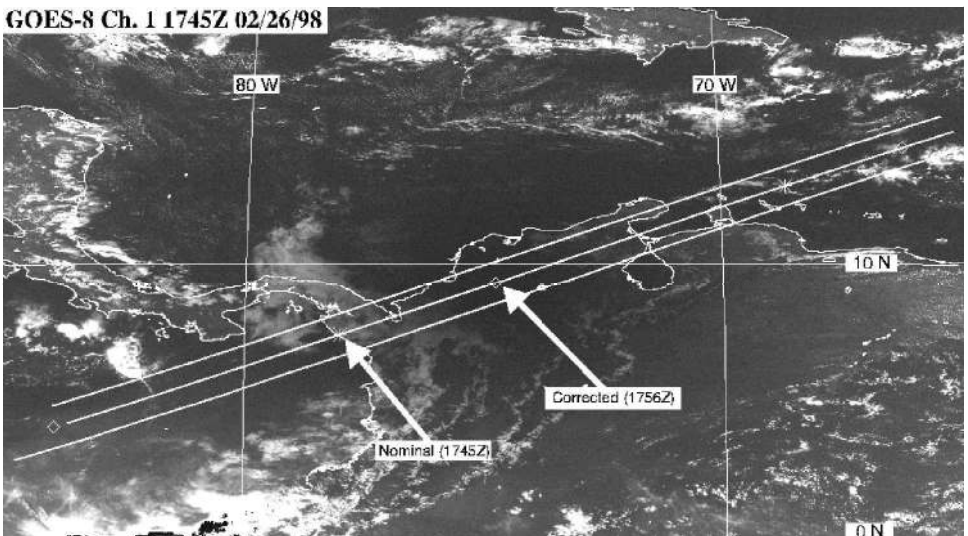

Figure 8.   Umbral advection correction applied to the GOES imagery data.
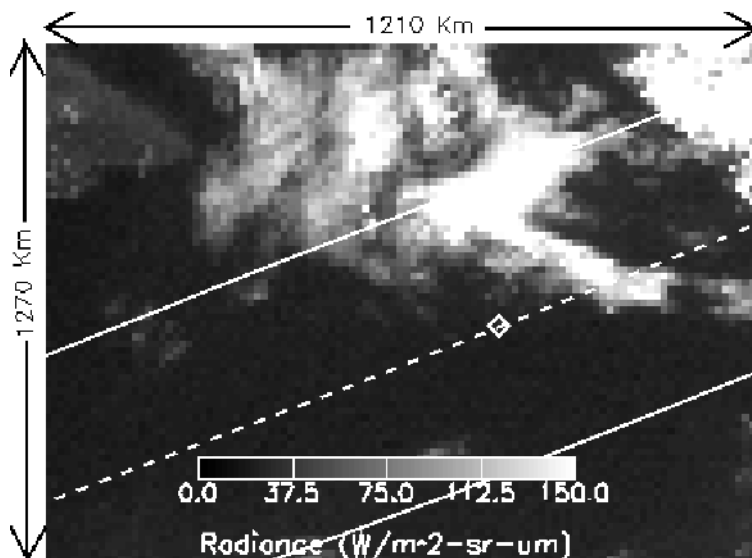
Figure 9. Local case study for GOES-K. Ch. 1 reflectance at 1630-Z (1 hr prior to eclipse). South-west and north-east corners of the image are at (3.4 S, 80.8 W) and (8.8 N, 68.8 W), respectively. Approximate dimensions (in km) are indicated on the edges of the image.

cloud), no deep convection was inferred, and cloud advection was minimal (contrary to what might be anticipated for upper-level cirrus), this cloud field was concluded to be of the marine stratocumulus variety. This is a desirable class for this application, as the thermal background field is not anticipated to change as drastically over the requisite temporal-differencing period.

The standard output of GOES detectors is a count value that is proportional to the amount of energy incident upon the detector surface. These counts are converted to the more familiar units of radiance or brightness temperature using calibration coefficients which depend on the instrumental, channel, and detector. While some vicarious calibrations are performed in-orbit (e.g. White Sands, New Mexico), most of these relationships are determined from pre-launch laboratory measurements calibrated against sources of known and tunable radiance. Imager calibration coefficients and formula were obtained directly from the National Oceanic and Atmospheric Administration (Weinreb *et al.* 1997).

The satellite claibration curves for GOES-K channels 1 and 2 are given in figure 10 along with the distribution of pixels in the scene before and during the solar eclipse. The peak in the pre-eclipse distribution for Ch. 1 is representative of ocean reflectance, while the extended tail describes cloudy pixels. The peak in the distribution is observed to shift downward in counts to sub-calibration levels and the tail of high counts vanishes during the eclipse. The small subset of pixels which contribute finite radiance to the eclipse curve are on the outskirts of the image (where the eclipse is not total). These pixels were filtered out for subsequent data analyses. The corresponding calibration and pixel distribution curves for Ch. 2 are shown in the lower panel of this same figure. The cloud component of the scene is revealed upon differencing the pre-eclipse and during-eclipse pixel count distributions. During the pre-eclipse (solar plus thermal) scene, a single peak is observed
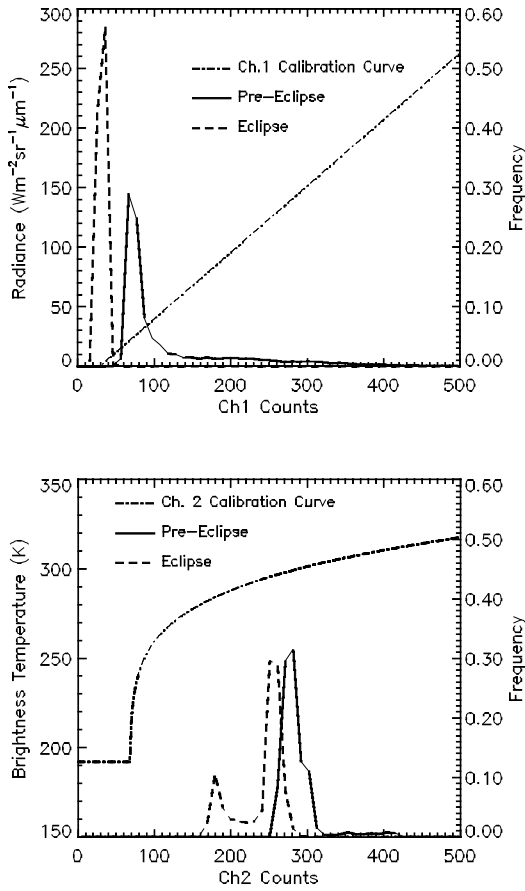
Figure 10. Calibration curves and scene pixel count distributions for the GOES-K case. Top panel: Ch. 1, Bottom panel: Ch. 2.

with a small number of larger counts. The eclipse distribution, which is equivalent to a night-time scene, is bi-modal (essentially the 'feet' of the Coakley and Bretherton 1982 arch plots based on spatial coherence techniques), as the cooler clouds stand apart from the warmer ocean surface scene.

Because temporal differences are performed on the Ch. 2 imagery in order to remove the thermal component of the scene, the condition of thermal invariance over the duration in question must be addressed. As mentioned above, the advection, formation and dissipation of clouds is usually non-negligible over an hour's time. For example, a cloud moving at $10 \, \mathrm{m \, s^{-1}}$ will travel $36 \, \mathrm{km}$ over the course of an hour, or roughly 9 pixels at the resolution of GOES-K Ch. 2. The optical properties of cumulus convection can also change significantly over this period. To assess the stability of the thermal background, temporal differences using the Ch. 4 (more sensitive to changes in cloud due to higher emittance as discussed) were performed. Figure 11 shows the (1630–1730 Z) difference in the Ch. 4 brightness temperature field. It is evident that for this case much of the cloud field exhibits a relatively stable ($\Delta T_{10.7} < 2.0 \mathrm{K}$) thermal background over this period, with a few pockets of exception near cloud edges. Of interest is the apparent dissipation (transition from cool to
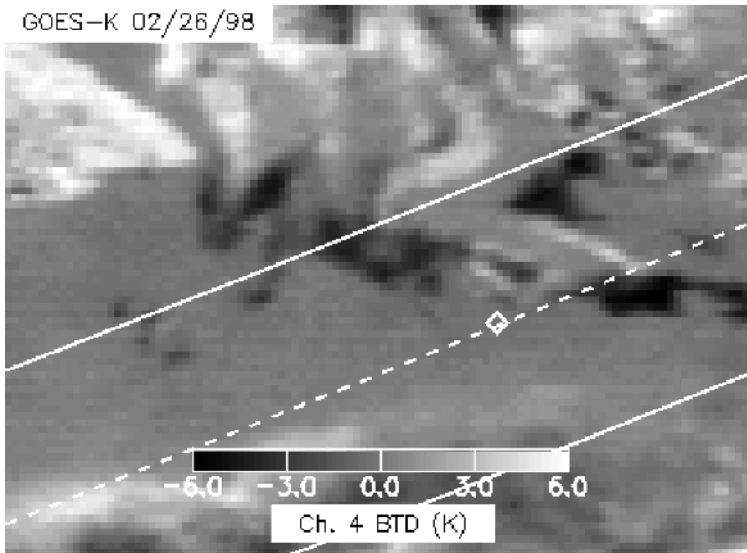
Figure 11. Change in the GOES-K 10.7 µm brightness temperatures before and during the eclipse (1630 Z–1730 Z) used in assessment of cloud thermal-field stability.

warm, or a 'negative signal' in the difference plot) of this cloud field as eclipse approaches. Dissipation as opposed to advection is inferred from the tongue of cloud near the sub-eclipse (diamond point in figure 11) as negative tendencies are observed to surround this cloud field. While this phenomeon has not been confirmed for these particular data, ground-based eclipse observers have noted the general dissipation of shallow clouds, presumably due to an increase in atmospheric stability, as the umbral shadow approaches (John Weaver (CIRA), personal communication).

For data analysis, several masks were applied to isolate cloud fields within the umbral shadow whose thermal field difference between the two times (as defined by the 10.7 µm channel-considered as unaffected by solar component) changed by less than 2 K in brightness temperature. The masking scheme employed is similar to that of Rao *et al.* 1995, with the additional constraints of a stable thermal background field ($\Delta(T(t_1, t_2)) \leqslant 2$ K) and zero-radiance in Ch. 1 during the eclipse. The resultant mask is shown in figure 12, where areas in white have been designated as valid cloud pixels to process. In the results to follow, scatter diagrams include only the masked-pixel subset of the imagery.

By performing a (1630–1730 Z) difference of the GOES-K Ch. 2 imagery, invoking the assumption of thermal invariance, and normalising by the transmission-weighted spectral flux, the visible reflectance of the scene was obtained according to equation (7). Figure 13 shows the result of this procedure for the marine stratus case study. The values of albedo were observed to range from near-zero (corresponding to the dark ocean surface) upwards to 0.16 in the brightest of cloud regions. There are the quantities sought by retrievals which assume either solar reflection or thermal emission (obtained from the Ch. 2 image itself during the eclipse) components exclusively. The triangular feature in the upper-left corner of the image is a land surface (Los Santos, Panama) which reflects strongly the 3.9 µm radiation in the less-vegetated areas. The cloud 3.9 µm albedo data comprised the benchmark against which approximations from the literature were compared.

Figure 12. Cloud mask used for GOES-K retrievals. White regions designate detected clouds with stable $(\Delta - T_{10.7}(t_1, t_2) < 2.0°\text{K})$ thermal background fields and zero-visible radiance at time t_2 (1730 Z, at time of total solar eclipse).
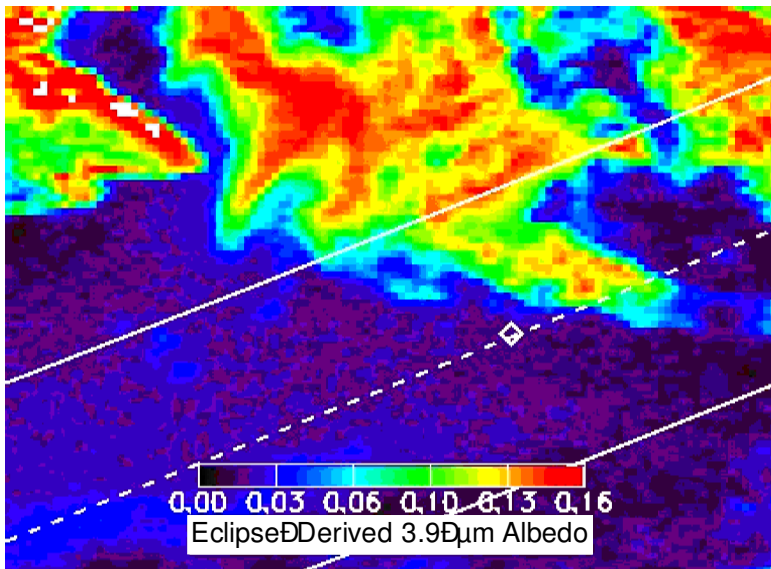

Figure 13   Eclipse-derived 3.9 μm albedo.

6.1. *Examination of existing methods*

Despite the ambiguity associated with daytime Ch. 2 imagery, several methods exist in the literature which apply resourceful methods to approximating these components (or even circumventing the problem altogether through iterative 'best-guess' approaches). Invariably, these estimation methods must invoke simplifying assumptions that lead to a departure from the true physics. While we do not attempt to address in detail all existing approaches here, a brief note on some of the more straight-forward empirical and theoretical approaches were included for direct comparison against albedo results derived from the eclipse data.

6.1.1. *Crude estimation*

It is first worthwhile to illustrate the inadequacy of using the Ch. 4 brightness temperature as a direct conversion to equivalent Ch. 2 radiance without regard to differences in cloud emittance between the two bands. The BTD between these two channels during the eclipse is shown as a function of the pre-eclipse visible radiance (a proxy for cloud optical depth) in figure 14. The low visible reflectivity tail corresponds to the ocean surface background, and the remaining points comprise the distribution of clouds. In the regions where the cloud is most optically thick (i.e. highest visible reflectance), the Ch. 4 brightness temperature is greater than that of Ch. 2 (negligible transmittance from the surface and a higher cloud emittance in Ch. 4). This agrees with the premise that Ch. 4 will emit more as a blackbody (a greater amount of radiation) than will Ch. 2 and hence yield a greater radiance value in the absence of upwelling transmission. At lower visible reflectance negative BTDs are observed owing to enhanced transmittance in Ch. 2 (allowing warmer surface
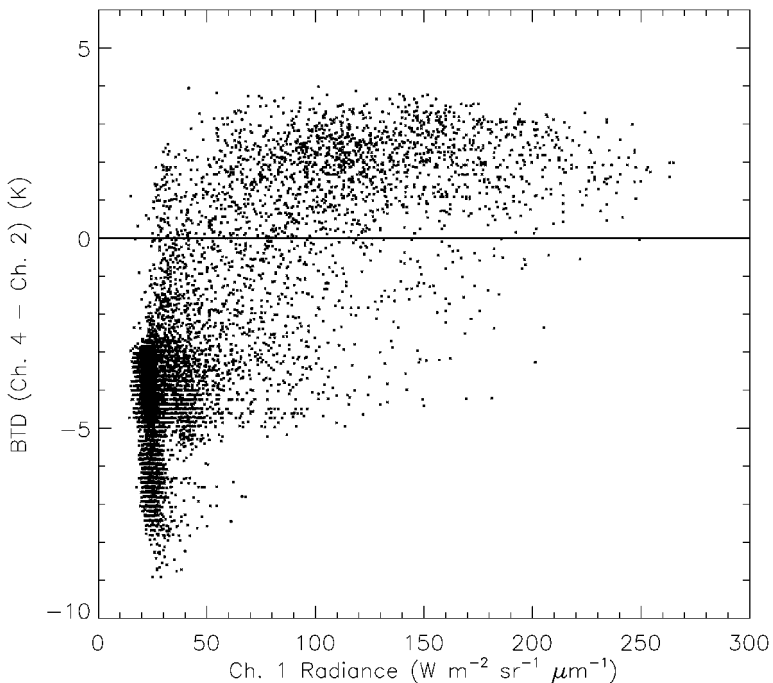

Figure 14. Brightness temperature difference (K) between Ch. 4 and Ch. 2 for GOES-K during the eclipse (1730).

emissions to contribute to the measurement). The Ch. 4 brightness temperature was used as input to the Planck function to evaluate an equivalent Ch. 2 thermal-only spectral radiance. For this exercise, the cloud emissivity in both channels was assumed (incorrectly) as unity.

Figure 15 compares this estimate against the eclipse-derived albedos. The plotted points in this scatter diagram (and all to follow) comprise the filtered imagery pixels (i.e. determined as being cloudy, having minimal change in $10.7\,\mu m$ thermal background, and without a detectable solar reflection component in the eclipse image). Overestimates of the $3.9\,\mu m$ albedo are observed than for optically thin clouds (i.e. lower values of reflectance). Because the $10.7\,\mu m$ emissivity is in fact larger than that of $3.9\,\mu m$, its brightness temperature will be slightly lower than that observed at $3.9\,\mu m$ (which is enhanced by surface emission contributions). Evaluating the Planck function with this cooler brightness temperature results in an underestimate of the true $3.9\,\mu m$ thermal component and in turn an overestimate of the visible component. Conversely, at larger optical depths (reflectance), emissions from below are effectively removed. The higher $10.7\,\mu m$ emissivity produces a larger radiance for a given cloud temperature. Applying this to the $3.9\,\mu m$ Planck function results in an overestimate of the thermal component, and hence an underestimate of the visible. Across this transition, there will exist an optical depth range where the approximation yields small-error. The agreement is not physically based; representing an instantaneous balance between opposing incorrect assumptions on spectral transmission and emissivity.
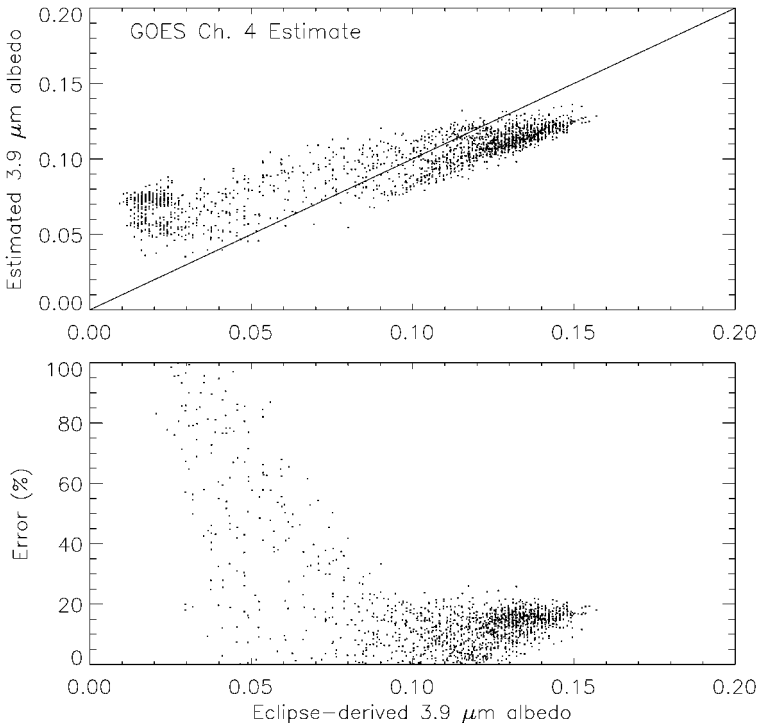

Figure 15. Comparison between eclipse-derived and $(B_{3.9}(T_{10.7}), \varepsilon_{3.9,\,10.7} = 1.0)$ albedo estimate (top panel) and corresponding relative percent error (bottom panel).

6.1.2. *Empirical relationships*

In their analysis of solar reflection off the sides of broken fields of low-level water clouds, Coakley and Davies 1986 develop an empirical method to remove the thermal component from the MIR daytime scene based on the relationship between AVHRR $11.0\,\mu$m and $3.7\,\mu$m thermal radiance from similar clouds observed at night. The sample data are taken from random observations of night-time AVHRR passes over the Pacific Ocean during the Northern Hemisphere (0 to 50° N) Fall. A fit is performed to a large number of bi-spectral measurements to yield an equivalent $3.9\,\mu$m radiance which is then subtracted from the daytime imagery. A power law relationship is obtained of the form

$$I_{thermal}(3.7\,\mu\text{m}) = 1.59 \times 10^{-7} I(11.0\,\mu\text{m})^{3.23} \tag{10}$$

where here the radiances are described in units of $\text{mW}\,\text{m}^{-2}\text{s}^{-1}\text{cm}^{-1}$. The AVHRR channels are considered here as equivalent to GOES Ch. 2 and Ch. 4 for comparisons with the eclipse data. Coakley and Davies 1986 acknowledge that there is no way to quantify these results for daytime observations directly. Their parameterisation was applied to the GOES eclipse data to attempt such a quantification.

Equation (10) was applied to the GOES-K Ch. 4 imagery to compute an estimate of the $3.9\,\mu$m thermal component. The corresponding visible component was obtained simply by taking the difference between the pre-eclipse radiance and this thermal-component estimate. Finally, the estimated visible radiance was applied to equation (7) to compute the $3.9\,\mu$m bi-directional cloud reflectance ($\rho_{3.9}$(cld)). Comparisons between this estimate and the eclipse-derived albedo (with a 1:1 correspondence line, for reference) along with relative percent error are shown in figure 16.

The best agreement was observed for clouds having higher $3.9\,\mu$m reflectivities (or lower $3.9\,\mu$m transmission), and the largest discrepancies occurred at lower cloud reflectivities. A strong negative slope of the scatter distribution (towards lower percent-error with higher cloud reflectance) was observed, with errors falling below 20% when $A_{eclipse}(3.9)$ exceeded roughly 0.15. The observed over-bias translates to an apparent underestimate of the parameterised thermal component, suggesting that the parameterisation may be tailored to optically thick clouds which do not allow a significant amount of thermal transmission from the warm lower boundary to transmit through and enhance the Ch. 2 thermal component. This would be consistent with the observations of best-performance in regions of optically thick cloud. Even here, however, underestimation of the thermal component was found to be on the order of 10%. This raises the additional possibility that the inherent differences between the AVHRR and corresponding GOES channels were too great to apply directly the same empirical fitting coefficients to the GOES imagery.

6.1.3. *Physically-based relationships*

Kaufman and Nakajima (1992) and Kidder *et al.* (1998) use simple constructs of radiative transfer theory to formulate a $3.9\,\mu$m albedo estimate applicable during either day or night. Whereas the former consider for their study AVHRR channels ($3.75\,\mu$m and $11.0\,\mu$m) and the latter GOES ($3.9\,\mu$m and $10.7\,\mu$m), the technique remains general to any similar instrument with similar window channels. Following GOES channel notation, the $3.9\,\mu$m albedo is given as

$$\rho_{3.9}(\text{cld}) = \frac{I_{3.9}(\text{obs}) - t'_{3.9}B_{3.9}(T_{10.7})}{t^o_{3.9}\pi^{-1}F_o\mu_o - t'_{3.9}B_{3.9}(T_{10.7})} \tag{11}$$
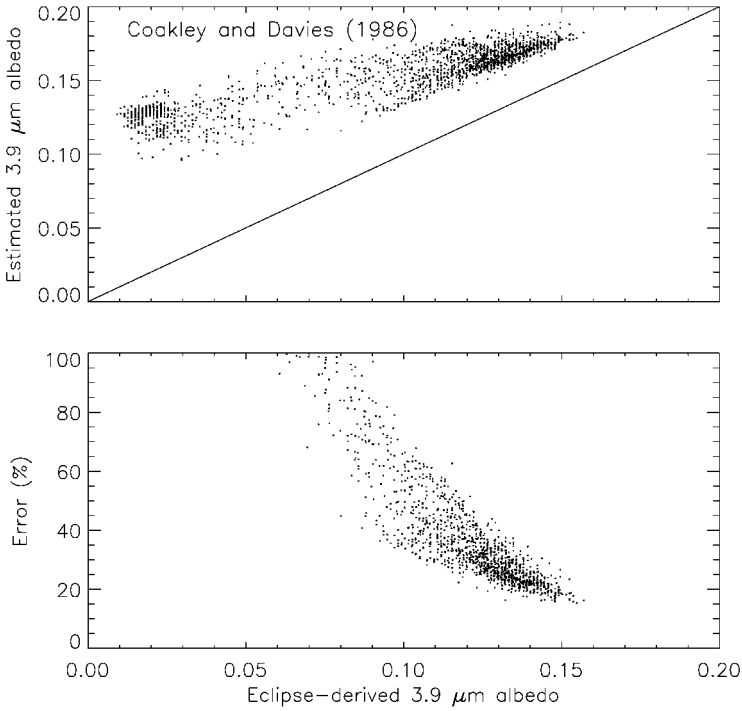
Figure 16.   Comparison between eclipse-derived and Coakley and Davies 1986 3.9 μm albedo estimate (top panel) and corresponding relative percent error (bottom panel).

where $A_{3.9}$ is the 3.9 μm albedo; $I_{3.9}$(obs) is the observed 3.9 μm radiance (solar plus thermal); $B_{3.9}(T_{10.7})$ is the equivalent blackbody emission at 3.9 μm based on the Ch. 4 brightness temperature measurement; and the transmission functions $t'_{3.9}$ (cloud to satellite) and $t^o_{3.9}$ (Sun to cloud, cloud to satellite) are dependent on the water vapour above cloud altitude. A fundamental assumption embedded within this relationship is that the clouds are of sufficient optical thickness such that their emittance (absorptance) and reflectance (albedo) sum to unity (i.e. negligible trans- mittance). King and Harshvardhan find this requirement to be satisfied for $\tau > 10.0$. The magnitude of error is therefore expected increase for optically thin clouds (especially cirrus, whose ambient temperatures are much colder than the potential upwelling transmission from levels below cloud base). An additional constraint that must be imposed in lieu of *a priori* assumptions is that the cloud reflects radiation isotropically (such that the solar/satellite geometry does not weigh into the detected radiance). This is not true in general, and azimuthal asymmetry effects becomes increasingly important with increasing solar zenith angle.

   The eclipse-derived and 3.9 μm estimated albedos and corresponding relative error are shown in figure 17. The superiority of a physically-based approach is evident especially at higher values of reflectivity, where errors fall below 5% for most clouds. The improved performance at large τ is anticipated, as this fulfils one of the assumptions implicit to the algorithm's formulation. Larger errors for lower reflecting clouds, while better than those of the previous estimate examples, reflect the fact that the algorithm is not equipped to handle cases where transmission from below the cloud is not negligible. These effects are expected to be exacerbated for cirrus,
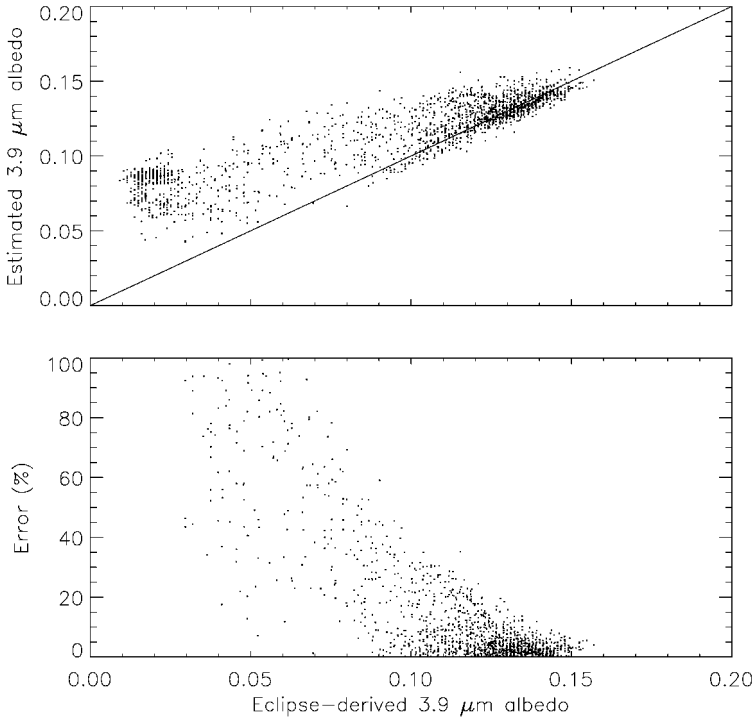
Figure 17. Comparison between (*a*) eclipse-derived and Kaufman and Nakajima 1986, Kidder *et al*. 1998, 3.9 μm albedo estimate and (*b*) corresponding relative percent error.

where the effects of transmission alter significantly the brightness temperatures estimated from satellite. It is by no coincidence that these represent the most poorly understood class of cloudiness, and this is where eclipse data has the greatest potential to yield new insight.

6.2. *Cloud optical property retrievals*

While total solar eclipses are not common occurrences, they are very predictable. If it is established that useful science information can in fact be obtained from them, the groundwork for a tailored experiment (e.g. one that includes active/passive sensors and *in situ* cloud micro-physical/optical-property measurements) could be laid out literally years in advance. One obvious benefit of such an effort would be the validation and improvement of existing remote-sensing based methods and parameterisations. In particular, cloud optical property retrievals making use of GOES Ch. 2 (or other instruments with channels in the middle IR) could be tested. Our ability to define atmospheric heating rates and a global surface/atmosphere energy budget hinges upon our ability to charactise properly these cloud optical properties on the global scale. To illustrate this point without venturing too far outside the germane, we attempted to apply the eclipse-derived GOES Ch. 2 visible reflectance to a simple physical cloud retrieval based on solar reflection alone.

Created for the purpose of retrieving cloud optical depth (τ) and effective particle radiance (r_{eff}) was a bi-spectral (isotropic reflectance at Ch. 2 plotted against that of Ch. 1) grid analogous to the discussion of figure 3. The grid structure, which is dependent on both the solar/observer geometry and wavelengths considered, was

constructed for the scene's mean observer and solar angles using a 16-stream radiative transfer model (Miller *et al.* 2000) and applied uniformly to all filtered (cloud mask, thermal stability, etc.) pixels in the image (the maximum variance for any of these angles from the mean for the entire scene was less than 5°). Plotted are the Ch. 1 and Ch. 2 bidirectional reflection functions as defined in equation (7). In the radiative transfer model, Ch. 2 radiances were computed without the thermal component (i.e. only the solar reflection component), as was supplied by the solar eclipse data. The surface albedos for Ch. 1 and Ch. 2 were approximated from the mean of a distribution of the observed clear-sky ocean surface reflectance. The 'retrieval' then entailed a simple over-plotting of the pixel data on the grids and interpolation between contours of constant optical depth and effective radii.

The bi-spectral retrieval grid with eclipse-derived reflectance data is shown in figure 18. The scatter of points indicates that clouds with a variety of optical properties exist in the scene. The majority of the distribution corresponds to a reasonable range of expected values for pristine marine stratus. There are many uncertainties associated with these physical retrievals, and it would require an additional paper to formally discuss them comprehensively. As such, this exercise should be considered more appropriately as a template from which to launch a more detailed study dedicated explicitly to the discipline of cloud property retrievals based on these eclipse data. The retrieval has been included here merely as a commentary on the utility of these eclipse data, and we do not intend to parlay these results as a final product to be considered as a standard for comparing against retrieval methods that decouple the 3.9 μm reflected visible component.
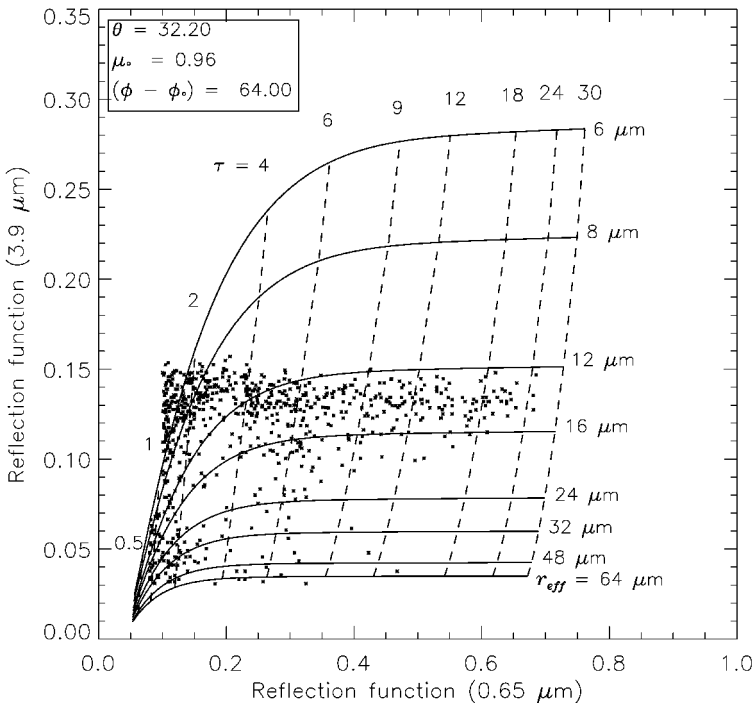

Figure 18.   GOES-K τ and r_{eff} retrievals.

7. Summary and conclusions

In this study, GOES imager data from the 26 February 1998 total solar eclipse have been used in a first attempt to decouple physically the solar and thermal components of the $3.9\,\mu m$ MIR imager channel. This decoupling required a one-hour Ch. 2 temporal difference which gave rise to errors associated with small-to-significant changes in the thermal background over this period. Appropriate cloud and thermal stability masks were applied to eliminate these pixels along with those having a finite visible component during the eclipse. The problem of the advection of the umbral shadow (leading to a mislocation of the central-eclipse point on the GOES imagery) was rectified by invoking a longitude/time cost function using the scan line information and computed eclipse positions. The differences in cloud droplet emittance between Ch. 4 and Ch. 2 were discussed shown to play a significant role in the interpretation of satellite cloud imagery.

GOES-K $3.9\,\mu m$ albedos were computed for a marine stratus layer located off the Western coast of Panama and near to the point of greatest eclipse. Results between eclipse-derived and existing physical/empirical methods in the literature were also presented and discussed for this case. The simplifying assumptions of an optically thick (such that transmittance is zero) cloud was shown to be a critical one for the approximations to perform well, as all estimates diverged significantly from eclipse-derived values at lower reflectivities. The physically-derived $3.9\,\mu m$ albedo (Kaufman and Nakajima 1992, Kidder *et al.* 1998) approximates reasonably the true albedo, as expected, when the simplifying assumptions associated with it are met. A cloud property retrieval was carried out using a simple bi-spectral grid approach following Nakajima and Nakajima (1995) created from a doubling and adding forward model described in Miller *et al.* (2000) to illustrate one potential application of these data to retrieval algorithm validations.

Although the point should be clear, it is emphasised that this work by no means encompasses the full range of possible experiments applicable to these eclipse data. The foremost intention of this work is to motivate future research in this area. In our ongoing struggle to better understand and quantify the complex nature of clouds in our atmosphere and their active role in the climate feedback system, the natural experiment afforded by total solar eclipses should not be left unexplored. It is, after all, the onus of the science community to seek out and take advantage of any and all possible avenues leading the expanding of knowledge. As total solar eclipses are very predictable events, the outline for a multi-sensor, multi-platform, and inter-disciplinary study could be outlined and refined conceivably years in advance to maximise the scientific information gained from these rare celestial events.

References

BECKER, F., and LI, Z.-L., 1990, Temperature-independent spectral indices in thermal infrared bands. *Remote Sensing of Environment*, **32**, 17–33.

COAKLEY, J. A., JR., and BRETHERTON, F. P., 1982, Cloud cover from high-resolution scanner data: Detecting and allowing for partially filled fields of view. *Journal of Geophysical Research*, **87**, 4917–4932.

COAKLEY, J. A., JR., and DAVIES, R., 1986, The effect of cloud sides on reflected solar radiation as deduced from satellite observations. *Journal of Atmospheric Science*, **43**, 1025–1035.

ESPENAK, F., 1998, *Fifty Year Canon of Solar Eclipses, 1986–2035* (Belmont, MA: Sky Publishing Corperation).

HANSEN, J. E., and TRAVIS, L. D., 1974, Near-infrared light scattering by terrestrial clouds. *Journal of Atmospheric Science*, **27**, 265–281.

Kaufman, Y. J., and Nakajima, T., 1993, Effect of Amazon smoke on cloud microphysics and albedo-analysis from satellite imagery. *Journal of Applied Meteorology*, **32**, 729–744.

Kidder, S. Q., Eis, K. E., and Vonder Haar, T. H., 1998, New GOES imager system products suitable for use on field-deployable systems. In *Proceedings: Battlespace Atmospheric and Cloud Impacts on Military Operations Conference, Air Force Research Laboratory, Hanscom Air Force Base, MA, 1–3 December 1995*, AFRL-VS-HA-TR-98-0103, Environmental Research Papers, No. 1217, pp. 452–459.

King, M. D., and Harshvardhan, 1986, Comparative accuracy of the albedo, transmission and absorption for selected radiative transfer approximations. NASA Reference Publication, **1160**.

Kleepsies, T. J., 1995, The retrieval of marine stratiform cloud properties form multiple observations in the 3.9 μm window under conditions of varying solar illumination. *Journal of Applied Meteorology*, **34**, 1512–1524.

Kratz, D. P., 1995, The correlated k-distribution technique as applied to the AVHRR channels. *Journal of Quantified Spectroscience and Radiative Transfer*, **53**, 501–517.

Li, Z.-L., and Becker, F., 1993, Feasibility of land surface temperature and emissivity determination from AVHRR data. *Remote Sensing of Environment*, **43**, 67–85.

Mason, J. W., and James, N. D., 1998, The total eclipse from Venezuela. *Journal of the British Astronomical Association*, **108**, 127–128.

Miller, S. D., Stephens, G. L., Drummond, C. K., Heidinger, A. K., and Partain, P. T., 2000, A multi-sensor diagnostic cloud property retrieval scheme. *Journal of Geophysical Research*, In press.

Nakajima, T. Y., and King, M. D., 1990, Determination of the optical thickness and effective particle radius of clouds from reflected solar radiation measurements. Part I: Theory. *Journal of Atmospheric Science*, **47**, 1878–1893.

Nakajima, T. Y., and Nakajima, T., 1995, Wide-area distribution of cloud microphysical properties from NOAA AVHRR measurements from FIRE and ASTEX regions. *Journal of Atmospheric Science*, **52**, 4043–4059.

Ou, S. C., Liou, K. N., Gooch, W. M., and Takano, Y., 1993, Remote sensing of cirrus cloud parameters using advanced very-high-resolution radiometer 3.7 and 10.9 μm channels. *Applied Optics*, **32**, 2171–2180.

Rao, N. X., Ou, S. C., and Liou, K. N., 1995, Removal of the solar component in AVHRR 3.7 μm radiances for the retrieval of cirrus cloud parameters. *Journal of Applied Meteorology*, **34**, 482–499.

Tanré, D., 1982, Interaction rayonnement-aérosols applications à la télédétection et au calcul du bilan radiatif, Thèse, Université des Sciences et Techniques de Lille.

Weinreb, M., Jamieson, M., Fulton, N., Chen, Y., Johnson, J. X., Bremer, J., Smith, C., and Baucom, J., 1997, Operational calibration of the imagers and sounders on the GOES-8 and -9 satellites. NOAA Technical Report NESDIS 44, US Dept. Commerce, National Oceanic and Atmospheric Administration, Washington, D.C.